

Grain boundary tracking technique: four-dimensional visualisation technique for determining grain boundary geometry with local strain mapping

Toda, Hiroyuki

Department of Mechanical Engineering, Kyushu University

Ohkawa, Yoshikazu

Department of Mechanical Engineering, Toyohashi University of Technology

Kamiko, Takanobu

Department of Mechanical Engineering, Toyohashi University of Technology

Naganuma, Takuma

Department of Mechanical Engineering, Toyohashi University of Technology

他

<https://hdl.handle.net/2324/1804189>

出版情報 : Acta Materialia. 61 (14), pp.5535-5548, 2013-04-01. ASM International
バージョン :
権利関係 :

Grain boundary tracking technique: four-dimensional visualisation technique for determining grain boundary geometry with local strain mapping

Hiroyuki Toda^{a,b}, Yoshikazu Ohkawa^b, Takanobu Kamiko^b, Takuma Naganuma^b,
Kentaro Uesugi^c, Akihisa Takeuchi^c, Yoshio Suzuki^c, Masakazu Kobayashi^b

^a [Department of Mechanical Engineering, Kyushu University, Nishi-ward, Fukuoka, FUKUOKA 819-0395, Japan](#)

^b Department of Mechanical Engineering, Toyohashi University of Technology, Toyohashi, AICHI 441-8580, Japan

^c Japan Synchrotron Radiation Research Institute, 1-1-1, Kouto, Mikazuki-cho, Sayo-gun, HYOGO 679-5198, Japan

Abstract

A procedure for determining three-dimensional grain boundary geometry and its change under external loading is proposed for evaluating crystallographic deformation behaviours in polycrystalline materials, and its feasibility is confirmed for an aluminium alloy. X-ray microtomography technique has been combined with gallium enhanced microscopy where grains are visualised in three dimensions by decorating grain boundaries with liquid gallium. Grain boundary particles are then extracted by comparing tomographic images with and without the gallium application. Three-dimensional reconstruction of grains is achieved using a connection scheme based on triplets of non-aligned points on grain boundaries. The deformation of the closed polygonal grains is visualised by combining the above technique with

microstructural tracking technique where the paths of particles are reconstructed by matching each pair of particles in consecutive images. This process also enables high-density four-dimensional strain mapping by tracking particles located in grains, providing direct interpretation of localised deformation caused by interaction between neighbouring grains.

Keywords: X-ray tomography, grain boundary, particle tracking, strain mapping, polycrystalline

1. Background

Almost all structural metals and alloys are used in a polycrystalline form. The mechanical response of polycrystalline aggregates is thus of primary importance in predicting texture development and macroscopic stress-strain response in polycrystalline materials that are undergoing plastic deformation. In conventional theories of crystal plasticity, various simplifications have been made to predict plastic deformation in polycrystalline materials. The representative assumption is that of homogeneous strain over a single grain, which has been introduced, for example, in the self-consistent model proposed by Budiansky and Wu [1]. Among the other common assumptions are simple and uniform grain shape and isotropy of the elastic and plastic responses of both crystal grains and aggregates.

The development of the EBSD (Electron Back Scattering Diffraction) technique and its application to polycrystalline materials have made it possible to quantitatively characterise the evolution of grains, subgrains and microtextures, as well as inhomogeneous strain distribution at the local scale [2]. It has been revealed that the evolution of inhomogeneous local strain gradients occurs, in many cases, along grain boundaries, together with a large variation in strain, which would correspond to the variation in dislocation density [3, 4]. Interesting morphological features have also been reported, such as the orientation subdivision of originally uniform grains during loading [5], and grain boundary migration due to the existence of inhomogeneous local strain gradients [6]. These observations strongly imply that such inhomogeneity and irregularity, which have not been considered in model analyses, are of crucial importance.

These observations are, however, two-dimensional, and their effectiveness as

representations of complex and irregular three-dimensional (3D) morphology and configuration in real structural materials has not been confirmed. For better understanding of actual 3D phenomena, the reconstruction of 3D information is needed. In light of this, the serial sectioning technique has been combined with EBSD to provide a methodology for such 3D microstructure reconstruction [7]. The principal disadvantage of the serial sectioning method is that it is fundamentally destructive, making it impossible to extend this technique to 4D (i.e., time axis and Euclidean space) observation. This technological limitation has prevented us from directly evaluating the time-spatial evolution of microstructure and microtexture in polycrystalline materials.

Recently some X-ray-diffraction-based techniques such as three dimensional X-ray diffraction (3DXRD) [8], diffraction contrast tomography (DCT) [9] and differential-aperture X-ray microscope [10], have been developed to quantitatively characterise polycrystalline materials in 3D/4D. For example, in 3DXRD, a rotating sample is illuminated with a monochromatic X-ray beam. All the X-ray diffraction spots recorded on a two-dimensional (2D) detector system are classified into groups belonging to identical grains, thereby depicting polycrystalline microstructure by generating a 3D map of local crystallographic orientation [8]. Techniques using X-ray diffraction are however sometimes vulnerable to spot overlap when a sample is subjected to plastic deformation.

This study proposes a form of indirect imaging of grains in polycrystalline materials on the basis of a high-resolution X-ray microtomography (XMT) technique. Grain boundary particles, which are often observed in high density in structural metals and alloys, are employed for the reconstruction of a given grain morphology as a high-dimensional polytope, typically with ~100 vertices for each grain. With this technique, 4D deformation of each grain can be rendered, together with mapping of 4D

local strain distribution. To confirm the feasibility of this technique, a high-resolution X-ray XMT technique has been used to obtain grain images in a wrought aluminium alloy. A detailed examination of the 4D characteristics of the crystallographic deformation behaviours is employed to discuss interactions among neighbouring grains during plastic deformation. The achievement of in situ observation of crystallographic deformation behaviours in 4D would be of significant value in the search for solutions to hitherto intractable problems in currently available model analyses.

2. Grain Boundary Tracking Technique

2.1 XMT technique and quantitative evaluations based on 3D/4D imaging

XMT offers a unique capability to determine the 3D character of internal microstructure and associated time evolution behaviours non-destructively. Third-generation synchrotron radiation (SR) facilities, such as SPring-8, have been identified as ideal platforms for XMT, providing a monochromatic X-ray beam with high photon flux and excellent lateral coherence [11]. XMT performed utilizing SR facilities has enabled the reconstruction of 3D volumes with a typical spatial resolution of 1 μm [12, 13], which has been achieved by an order of magnitude improvement in spatial resolution over a decade and a half. This remarkable improvement has enhanced the quality of reconstructed 3D images, and the accuracy of subsequent quantitative image analysis, thereby enabling the development of a variety of applied techniques, such as mappings of crack driving force [14, 15, 16], strain [17, 18, 19, 20, 21] and chemical concentration [22, 23], in 4D.

Owing to the high spatial resolution, the number of microstructural features, such as particles and microscopic defects (such as micropores), amounts to roughly

8,000 – 70,000 per 1 mm³ (with a typical field of view of 0.3 ~ 0.5 mm³ for a 1 µm spatial resolution set-up) in the case of wrought aluminium alloys [24, 25]. The present authors have proposed a microstructural tracking technique in which the physical displacements of microstructural features during external loading are utilised to compute the spatial distribution of mechanical quantities, such as strain and crack driving force, with down to a few micrometer spatial resolution [15, 17, 18, 19, 25]. Matching corresponding microstructural features accurately in consecutive frames is of crucial importance. Morphological characteristics of each microstructural feature (e.g., surface area, volume and gravity centre) are utilised, together with an appropriate trajectory prediction method and/or local pattern matching technique where necessary [17, 26]. The details of the microstructural tracking technique are available elsewhere [17].

In the case of strain mapping, the Delaunay tessellation algorithm [27] is then applied to generate an aggregate of space-filling irregular tetrahedra for obtaining local strain distribution. The gravity centres of all the microstructural features that have been successfully tracked are assigned as the vertex coordinates of tetrahedra, and local strain is calculated by interpolating a displacement field inside each tetrahedron.

2.2 Grain boundary tracking technique

2.2.1 General outline

XMT can achieve 4D observation with reasonable spatial resolution and relatively large specimen size. As the first step in the grain boundary tracking (hereinafter GBT) process, the deformation behaviour of a miniaturised specimen is observed in situ in 4D with the XMT technique, as shown schematically in Fig. 1 (a). A specially designed test rig mounted on a rotation stage for XMT is usually utilised for

the in-situ observation of the deformation and fracture process [15, 16, 19, 25]. The mechanical test must be interrupted before the final rupture occurs. The grain boundary wetting technique is then applied to the specimen, as shown in Fig. 1 (a) [28, 29]. In the case of aluminium and its alloys, liquid gallium is usually applied to the specimen surface, and the specimen is then maintained at an appropriate temperature for a certain period of time (typically 323 K for 500 sec, for gallium into Al) to diffuse gallium into the grain boundaries of the aluminium alloy. Finally, the gallium-decorated grain boundaries are scanned with the same XMT set-up. Thin bands with high X-ray absorption in the image are identified as grain boundaries. Even if an appropriate element that can decorate grain boundaries is not available, film-like grain boundary precipitates, which are sometimes observed in various alloys, may be used in the same way.

Precise image registration is performed between the tomographic images captured before and after gallium application. A 3D marker-based registration, in which microstructural features are used as markers, is performed to calculate necessary image shifts. The registration consists of a rigid transformation (rotation and translation in all directions) combined with isotropic scaling to model a small percentage of expansion due to gallium application [30].

After selecting an appropriate threshold for the linear absorption coefficient, the 3D gallium image is segmented on a slice-by-slice basis for the whole 3D image stack. The obtained set of binary grain boundary images is used for masking purposes, as shown schematically in Fig. 2 (a) and (b), and the microstructural features are classified into grain boundary and grain interior with respect to their gravity centre locations, as shown in Fig. 2 (c) and (d). Each grain is reconstructed as a polygon mesh using the extracted microstructural features located along the grain boundaries. In this

process, a given set of these features is represented as vertices for each grain, which are three-dimensionally connected by plane triangles to create a 3D grain mesh without overlaps and gaps, as shown in Fig. 2 (e). The polygon mesh actually represents the outer contour of a grain (i.e., the grain boundary). **In order to obtain reasonable information from the reconstructed polycrystalline microstructure, a sufficient number of microstructural features that are larger in size than the spatial resolution level of an XMT set-up is required.**

The aforementioned microstructural tracking technique is then applied both to the microstructural features located along the grain boundary and to those located in the grain interior. The deformation process of each polygonal grain is reproduced by tracking the microstructural features located along the grain boundaries, as shown in Fig. 1 (b). High-density 4D strain mapping is achieved by tracking the microstructural features located in the grain interior, as shown in Fig. 1 (c) and Fig. 2 (f), enabling the assessment of inhomogeneous strain distribution in each grain. The combination of the morphological information on the grains and the 4D strain mapping offers a direct method of assessing the fundamental deformation mechanisms of polycrystalline materials, such as the strong interaction between neighbouring grains.

2.2.2 Details of grain segmentation

2.2.2.1 Masking treatment

Gallium-decorated bands that correspond to the grain boundaries are segmented, after eliminating a matrix alloy and microstructural features which typically have linear absorption coefficients different from the gallium-decorated grain boundary, by selecting appropriate threshold values for the linear absorption coefficient. In order to perform this precisely, two binary images of the identical region are prepared with different gray-scale ranges and threshold values. For example, in the subsequent

experiment described in section 3.11, a linear absorption coefficient range, $\Delta\mu$, of 0 ~ 100 cm⁻¹ (which [has been mapped to a 8-bit](#) gray-scale between 0 and 255), and a threshold value, μ_c , of 23.5 cm⁻¹, were used to obtain an image data set in which both gallium-decorated grain boundaries and dispersion particles are clearly visualised, as shown in Fig. 3 (a). On the other hand, a $\Delta\mu$ of 35 ~ 135 cm⁻¹ and μ_c of 74.2 cm⁻¹ were applied in the case shown in Fig. 3 (b), in which dispersion particles and part of the gallium-decorated grain boundaries are almost eliminated. This is because each constituent particle has a relatively sharp linear absorption coefficient peak, simply owing to its stoichiometric composition (in this case, ~ 74.2 cm⁻¹), whereas the gallium-decorated grain boundary shows a wide linear absorption coefficient range depending on the local extent of gallium diffusion [29]. The gallium-decorated grain boundary alone is therefore successfully extracted by extracting regions that partially overlap between the two binary images, by means of an image processing algorithm, as shown in Fig. 3 (c) [31]. As a matter of course, $\Delta\mu$, and μ_c must be calibrated depending on the extent of gallium penetration and the species of dispersion particles embedded in the respective alloys.

Usually gallium penetration is not uniform and continuous, because grain boundary character [29, 32, 33] and internal stress [34] significantly affect penetration behaviour. It has been claimed that penetration does not occur in low-angle grain boundaries, and that not all high-angle grain boundaries are necessarily able to be decorated by gallium [29]. In order to obtain reasonable gallium-decorated grain boundary images for masking, then, dilation and erosion [35] are performed to connect discontinuous grain boundaries, as shown in Fig. 3 (d). A region that is three-dimensionally enclosed by a grain boundary network is then identified as a domain corresponding to each crystallographic grain, as shown in Fig. 3 (e).

2.2.2.2 Recovery of missing grain boundary

As mentioned above, the grain boundary is not completely visualised with gallium penetration on physical grounds alone. In addition, the above-mentioned combination of dilation and erosion can be effective only for partly disconnected grain boundary planes with small (i.e., within a few voxels) gaps.

In order to detect partly perforated grain boundaries that are unknown a priori, the marker-controlled watershed algorithm [35, 36] is employed where necessary, as shown in Fig. 4 (e). The material used for Figs. 4 and 5 is an AA5083 alloy with an equiaxed grain structure. In the watershed transformation, a 2D image is assumed as a topographic relief which is then flooded from a previously defined set of markers. A water source is placed in each regional minimum. In order to implement this algorithm in the binarised gallium-decorated grain boundary image, the topographic relief is produced by employing the distance transform algorithm [35, 36], as shown in Fig. 4 (c), which provides a grey level image in which grey level intensity represents the distance to the closest grain boundary from each point. By applying the watershed algorithm to a distance-transformed binarised image, the grain boundary line is drawn as a partition that prevents water coming from different sources from merging.

In practice, the watershed transform typically produces over-segmentation [35] due to the existence of image noise or irregular and complex structure in the gradient image, as shown by yellow arrows in Fig. 4 (a). One of the typical causes of over-segmentation is an image artefact due to X-ray deflection, such as is shown in Fig. 4 (f) by white arrows. To suppress the over-segmentation originating from image noise, two kinds of image filtering are applied. First, as a basic and simple noise reduction scheme, only features over a certain 3D volume (typically 27 ~ 5,000 voxels) are accepted as grain boundary, as shown in Fig. 4 (b). Second, a filtering method called

h -minima transform [36], shown in Fig. 4 (d), is simultaneously applied, and this removes spurious grey value minima whose dynamic is less than or equal to a given threshold, h , while the rest of the information remains intact. The obtained set of 2D binary grain boundary images are used for masking purposes, as shown in Fig. 2 (a) and (b).

Figure 5 represents a typical example of the watershed-transform-treated image shown in 3D. It clearly demonstrates that an ill-segmented grain boundary which has only been partly reconstructed (roughly 50 % in this case) can be recovered successfully by optimising a few parameters in the segmentation processes.

3. Demonstration of GBT technique on a practical aluminium alloy

3.1 Experimental and image processing methods

3.1.1 Synchrotron experiment

The specimen used for tomographic observation was taken from a rolled plate of 2024 aluminium alloy that was solution heat-treated at 768 K for 36 ks (furnace cooling), and then ageing treated at 523 K for 216 ks. Typical grain size was 100 ~ 150 μm on the L-T plane, and 80 μm in the thickness direction. The diameter of the dispersion particles, which play a key role in the GBT technique, ranged between 3 and 8 μm . A single-edge notched tensile specimen of 19 mm \times 0.6 mm \times 0.6 mm was tested in the L-T orientation.

A high-resolution XMT experiment was performed using the X-ray imaging beamline, BL47XU, of the Japanese synchrotron radiation facility, SPring-8. A material test rig specially designed for XMT was positioned approximately 49 m from the X-ray source. The test rig controller had a load resolution of 0.1 N, which made it possible to

undertake well-controlled quasi-static material tests using the miniaturised specimens. The test rig exhibited a displacement stability of about $0.1 \sim 0.2 \mu\text{m}$, thereby enabling the production of tomographic scans with almost no blurring caused by specimen wobble. A monochromatic X-ray beam with a photon energy of 20 keV, generated by a liquid nitrogen-cooled Si (111) double crystal monochromator, was used. An image detector consisted of a cooled $4000 \text{ (H)} \times 2624 \text{ (V)}$ element CCD camera (effective pixel size: $5.9 \mu\text{m}$) used in 2×2 binning mode, a single crystal scintillator ($\text{Lu}_2\text{SiO}_5\text{:Ce}$), and a lens ($\times 20$). The image detector was positioned 55 mm behind the sample, thereby rendering the imaging system sensitive to phase modulation [11]. The in situ loading stage allowed the specimen to be scanned under monotonic tensile loading.

Figure 6 shows a nominal stress - nominal strain curve obtained during the tensile test. The first tomographic scan was performed without loading, and the subsequent 5 scans were performed during loading at nominal strain of about 0.5, 1.0, 1.3, 1.8 and 2.3 %, respectively. To suppress image blurring caused by relaxation behaviour during scanning, displacement was fixed at the above strain levels for 20 min. before each scan. After the 5th scan, which was immediately prior to the final rupture, the specimen was dismounted from the test rig, and the liquid gallium wetting technique was applied to the specimen. After this, further scanning was performed, to characterise grain structure, with a sample-to-detector distance of 10 mm. A total of 1,500 radiographs, scanning 180 degrees in 0.12-degree increments, were obtained in each scan. The entire cross-section of the specimen, and a region about $626 \mu\text{m}$ high, were captured on the CCD camera. Image slices were reconstructed from a series of projections based on the conventional filtered backprojection algorithm [37]. An isotropic voxel with a $0.5 \mu\text{m}$ edge was achieved in the reconstructed slices.

3.1.2 Details of the image processing procedures

Micron-level dispersion particles embedded in 2024 aluminium alloys have been reported to be mainly equilibrium S-Al₂CuMg phase with some amount of Al-Cu-Si-Fe-Mn phase expressed as (Fe,Mn)_xSi(Al,Cu)_y (typically, $x \approx 3$ and $y \approx 11$) [38, 39]. Usually Al₂Cu is mainly observed in the form of small precipitates [38]. The linear absorption coefficient values of α -aluminium, θ -Al₂Cu, S-Al₂CuMg and gallium are 8.6, 84.9, 59.1 and 239.3 cm⁻¹, respectively, at an X-ray energy of 20 keV. The linear absorption coefficient value of the gallium-decorated grain boundary varied between approximately 35 and 135 cm⁻¹, suggesting a wide variation in local gallium concentration in the grain boundary [29]. Two sets of 8-bit gray-scale images were prepared, as described in Section 2.2.2.1. The gray value in each dataset was calibrated so that the linear absorption coefficients of 0 ~ 100 and 35 ~ 135 cm⁻¹ fell within an 8-bit gray-scale range between 0 and 255.

To estimate the volume of each dispersion particle with sub-voxel accuracy, faceted iso-intensity surfaces of pentagonal shape (which is **required** for accurate microstructural tracking) were computed from the volumetric data set using the conventional Marching Cubes algorithm [40]. To suppress inaccuracies originating from image noise, only particles over 23.168 voxels in volume were counted as particles in the quantitative analysis. Volume, V , surface area, A , and the centre of gravity are measured in the tomographic images.

Precise image registration was then performed before the particles were tracked, using a transformation matrix, which minimises the sum of the distances between identical microstructural features captured at neighbouring scan steps. The particles were tracked throughout tensile loading by employing the matching parameter method with the modified spring model [26]. The coefficients α , β and γ in the matching probability parameter used in reference [26] were determined as 0.8, 0.1 and

0.1, respectively, after systematically searching for the optimal condition in a preliminary trial. The other details of the microstructural tracking and 3D strain mapping procedures are available elsewhere [26].

3.2 Example of GBT technique

An illustration of dispersion particles belonging to a specific crystal grain is shown in Fig. 7 (a) and (b). These particles have been classified into grain boundary and grain interior varieties by means of the masking treatment involving a gallium-decorated grain boundary image, as shown in Fig. 7 (c). Particles located on the grain boundary (Fig. 7 (a)) have been used to reconstruct the morphology of a given crystal grain as a polygon mesh (Fig. 7 (d)). In the case of this specific grain, there were 170 grain boundary Al_2Cu particles, with an average diameter of 6.0 μm . The approximate shape of this grain can be visualised using these particles. Since this image consists of three-dimensionally connected triangles that express the outer contours of a given crystal grain, it can be volume-rendered, as shown in Fig. 7 (e), where stereoscopic shadow processing has been applied to the original polygon mesh.

As described above, particles located in the grain interior have been used for measuring internal strain, as shown in Fig. 8, where four grains have been sampled and variations in normal strain in the tensile direction are expressed in the form of histograms. It is interesting to note that, although the macroscopic applied load is tensile in nature, compressive strain is locally seen in Fig. 8. The increments of macroscopic applied strain were 0.005, 0.010, 0.013, 0.018 and 0.023, for loading steps 1, 2, 3, 4 and 5, respectively, while the measured local strain increment varied widely between -0.1 and $+0.2$. It is noteworthy that when the same sample was scanned twice without applying any external load, the full width at half maximum (FWHM) in normal strain

distribution were 0.0052 and its average was 0.00. On the other hand, FWHM varies between 0.079 (Grain 4) and 0.110 (Grain 3) in Fig.8. The wide variation seen in Fig. 8 is therefore attributable to inherent variation in local strain. Fig. 9 shows virtual cross-sections at which relatively large internal strain was observed. One-dimensional strain values between particles P_1 and P_2 , P_1 and P_3 , and P_2 and P_3 are 0.108, 0.112 and 0.209, respectively, which corresponds to average equivalent strain, $\varepsilon_{eqv} = 0.185$ in the tetrahedron that consists of four vertices including particles P_1 , P_2 and P_3 . This implies that local strain varies significantly among neighbouring particle pairs to this extent.

It is characteristic that **an increase in height and decrease in width** are observed at the same time, in all the grains, after loading step 3. The strain distribution in each grain also varies with loading. For example, Grain 3 exhibits asymmetric strain distribution with very large compressive and tensile strain values, alternately observed, with loading. These behaviours would appear to reflect complex interaction among neighbouring grains, with severe alteration under loading conditions. It is reasonable to assume that grains with low Taylor factors are subject to intensive deformation by neighbouring grains with comparatively high Taylor factors [41]. It is well known that dislocation cell structure within each grain is strongly affected by the grain's orientation [42]. The remarkably heterogeneous deformation among the grains is typically accompanied by the formation of deformation band and/or grain sub-division [41, 43].

Fig. 10 shows the outer contours of Grain 4 (from Fig. 8), reconstructed in the form of a polygon mesh. The morphological change in Grain 4 during loading is also shown, together with 4D strain mapping on a virtual cross-section. Since the amount of applied strain is relatively small in this study, Fig. 10 does not show any significant change in grain morphology. The physical displacement of the vertices of each grain boundary polygon (which correspond to grain boundary particles), during external

loading, are magnified and shown in Fig. 11. Large compressive (i.e., inward) and tensile (i.e., outward) displacements are observable on the grain boundaries. Clusters of arrows similar in direction and size indicate interfaces with neighbouring grains. Large generated strain may be observed [in regions close to the grain boundary](#) in Fig. 10, corresponding to the large tensile displacement seen on the grain boundary in Fig. 11. It is reasonable to assume that such large strain concentration and grain boundary displacement arises from a mismatch in deformability among neighbouring grains. Grain boundary displacement also varies with loading, in a complex manner, sometimes resulting in a reversal of compression and tension. This may also be attributable to significant mutual interaction among neighbouring grains, which might vary with loading.

In order to visualise the interaction among the three grains shown in Fig. 8 (Grain 1, Grain 2 and Grain 3), various strain components, as well as the ratio of equivalent and hydrostatic strains, [which is sometimes associated with void growth \[18,44\]](#), are shown in Fig. 12. Here, the dotted lines show grain boundaries. In order to investigate three-dimensional interaction among the three grains, three parallel virtual cross-sections (specified in Fig. 13 (a)) are shown in Fig. 13 (b) – (d), together with the distributions in the ratio of equivalent and hydrostatic strains. It is interesting to note that, although the macroscopic applied load is tensile in nature, blue and blue-green regions are seen in Fig. 12 (a), indicating that some regions are locally exposed to compression. Even in the compressive regions, the extent of compression varies up to -0.217 in axial strain in the loading direction, for the macroscopic strain increment of 0.023. Inhomogeneous strain distribution is especially notable around the top of Grain 1, across the interface between Grains 2 and 3, and around a quarter from the top of Grain 3. All these locations correspond to sites with adjacent transverse grain

boundaries of neighbouring grains. A region of large strain is observed to be distributed extensively across the grain boundaries. Although the average hydrostatic strain of the respective grains is almost zero, patches of relatively large hydrostatic strain are observable in all three grains, where a fairly large ratio of equivalent and hydrostatic strains are simultaneously observable. It can be inferred that void nucleation and growth are promoted at such locations. Fig. 13 suggests that such high triaxiality regions are restricted to three-dimensionally **small regions** between neighbouring grains.

4. Conclusion

Projection-type XMT is confined to a spatial resolution limit of about 1 μm , making it impossible to visualise nanoscopic microstructural features such as grain boundary morphology. Although the grain boundary wetting technique enables the visualisation of decorated grain boundaries that can be scanned using the XMT technique, it is fundamentally destructive, causing brittle fractures in treated specimens. This study proposed a grain boundary tracking technique in which grain boundary particles are employed in the reconstruction of a given grain morphology as a high-dimensional polytope. 4D deformation of respective grains can be rendered below the medium temperature range, where grain boundary migration does not occur from initial grain boundary particles. With this technique, high density mapping of 4D local strain distribution is also achieved, which offers a robust tool for analysing localised strain distribution due to crystallographic deformation behaviour in polycrystalline materials. Crystal grains in practical polycrystalline materials typically exhibit a highly irregular and complex morphology, which is here reconstructed without overlapping and gaps, in the manner of a jigsaw puzzle. The grain boundary tracking technique thus

offers a unique observational technique for investigating changes in such complex grain structure during deformation [that arises from interaction among neighbouring grains](#). The feasibility of the technique has been confirmed by applying it to the study of tensile deformation in a functional aluminium alloy, revealing strong and complex interaction among neighbouring grains during plastic deformation.

[The alternative methods for 3D grain identification, which are based on X-ray diffraction](#), have been reported in the literature, including 3DXRD [8] and DCT [9]. Although such X-ray diffraction-based approaches are relatively vulnerable to plastic deformation due to the spreading of diffraction spots, they appear to offer significant advantages to [the present GBT technique in that they provide access to crystallographic characteristics such as orientation and elastic strain](#). Recently Li et al., has demonstrated [that samples which have undergone plastic deformation of up to 6% percent have been successfully reconstructed using a technique related to 3DXRD \[45\]](#). As a promising extension of the present GBT technique, we have attempted to combine the technique with a special X-ray diffraction experiment, before or after a given GBT experiment [46]. If this combined technique can be successfully developed, the GBT technique would offer a yet more powerful tool for elucidating still poorly understood complex deformation behaviour of polycrystalline materials, from a crystallographic point of view.

Acknowledgements

The SR experiment was performed with the approval of JASRI, through proposal numbers 2005B0019, 2007B1213, 2008A1498 and 2009A1554. This work was undertaken partly with the support of a Grant-in-Aid for Scientific Research (A) from JSPS, through subject No. 20760466. The authors also appreciate the financial

assistance of the Light Metal Educational Foundation.

Reference

- [1] Budiansky B, Wu T Y. Proc 4th US Nat Congr Appl Mech 1962; 1175.
- [2] Mishra R, Kubic R. Microscopy and Microanalysis 2008; 14: 552-553.
- [3] Wang Y, Shao W Z, Zhen L. Materials Science and Engineering A 2008; 497: 479-486.
- [4] Zhong Y, Yin F, Sakaguchi T, Nagai K, Yang K. Acta Mater 2007; 55: 2747-2756.
- [5] Sandim H R Z, Raabe D. Scripta Materialia 2005; 53: 207-212.
- [6] Hasegawa M, Yamamoto M, Fukutomi H. Acta Mater 2003; 51: 3939-3950.
- [7] Adachi Y, Morooka S, Nakajima K, Sugimoto Y. Acta Mater 2008; 56: 5995-6002.
- [8] Poulsen H F, Three Dimensional X-Ray Diffraction Microscopy. Springer, 2004.
- [9] Ludwig W, Schmidt S, Lauridsen E M, Poulsen H F, Applied Crystallography 2008; 41: 302-309.
- [10] Larson B C, Yang W, Ice G, Budai J, Tischer J, Nature 2002; 415: 887-890.
- [11] Cloetens P, Pateyron-Salome M, Buffière J Y, Peix G, Baruchel J, Peyrin F, Schlenker M. J Appl Phys 1997; 81: 5878.
- [12] Uesugi K, Suzuki Y, Yagi N, Tsuchiyama A, Nakano T. Nuclear Instruments and Methods in Physics Research Section A 2001; 467-468: 853-856.
- [13] Buffière J Y, Maire E, Cloetens P, Lormand G, Fougères R. Acta Mater 1999; 47: 1613-1625.
- [14] Ferrié E, Buffière J Y, Ludwig W, Gravouil A, Edwards L. Acta Mater 2006; 54: 1111-1122.
- [15] Toda H, Sinclair I, Buffière J Y, Maire E, Khor K H, Gregson P, Kobayashi T. Acta Mater 2004; 52: 1305-1317.

- [16] Toda H, Yamamoto S, Kobayashi M, Uesugi K. *Acta Mater*, 2008; 56: 6027-6039.
- [17] Toda H, Maire E, Aoki Y, Kobayashi M. *J Strain Analysis* 2011; 46: 549-561.
- [18] Toda H, Yamaguchi T, Nakazawa M, Aoki Y, Uesugi K, Suzuki Y, Kobayashi M. *Mater Trans* 2010; 51: 1288-1295.
- [19] Toda H, Minami K, Koyama K, Ichitani K, Kobayashi M, Uesugi K, Suzuki Y. *Acta Mater* 2009; 57: 4391-4403.
- [20] Hild F, Roux S. *Strain* 2006; 42: 69-80.
- [21] Bay B. *Strain Analysis* 2008; 43: 745-760.
- [22] Toda H, Nishimura T, Uesugi K, Suzuki Y, Kobayashi M. *Acta Mater* 2010; 58: 2014-2025.
- [23] Ikeda S, Nakano T, Tsuchiyama A, Uesugi K, Suzuki Y, Nakamura K, Nakashima Y, Yoshida H. *Americam Mineralogist* 2004; 89: 1304-1312.
- [24] Masuda S, Toda H, Aoyama S, Orii S, Ueda S, Kobayashi M. *J Japan Foundry Engng Soc.* 2009; 81: 312-319.
- [25] Toda H, Maire E, Yamauchi S, Tsuruta H, Hiramatsu T, Kobayashi M. *Acta Mater*, 2011; 59: 1995-2008.
- [26] Kobayashi M, Toda H, Kawai Y, Ohgaki T, Uesugi K, Wilkinson DS, Kobayashi T, Aoki Y, Nakazawa M. *Acta Mater.* 2008; 56: 2167-2181.
- [27] Barber C B, Dobkin D P, Huhdanpaa H T. *ACM Transactions on Mathematical Software* 1996; 22: 469-483.
- [28] Ludwig W, Bellet D. *Materials Science and Engineering A* 2000; 281: 198-203.
- [29] Kobayashi M, Toda H, Uesugi K, Ohgaki T, Kobayashi T, Takayama Y, Ahn B G. *Philos Mag* 2006;86:4351-4366
- [30] Ohgaki T, Toda H, Sinclair I, Buffière J Y, Ludwig W, Kobayashi T, Niinomi M, Akahori T. *Materials Science and Engineering A* 2005; 406: 261-267.

- [31] Russ J C. The Image Processing Handbook 2nd ed. CRC Press 1995.
- [32] Volovitch P, Traskine V, Baudin T, Barrallier L. Interface Sci. 2002; 10: 303.
- [33] Wynblatt P, Takashima M. Interface Sci. 2001; 9: 265.
- [34] Larikov L N, Prokopenko G I, Franchuk V I, Yakubtsov I A. Materials Science 1990; 26: 247-251.
- [35] Dougherty E R, Lotufo R A. Hands-on Morphological Image Processing. SPIE PRESS; 2003.
- [36] Ohser J, Schladitz K. 3D Images of Materials Structures: Processing and Analysis. Wiley-VCH Verlag; 2009.
- [37] Herman G T. Image reconstruction from projections: the fundamentals of computerised tomography. Orland: Academic Press; 1980.
- [38] Son I J, Nakano H, Oue S, Kobayashi S, Fukushima H, Horita Z. Trans Nonferrous Met Soc China. 2009; 19: 904-908.
- [39] Gao M, Feng C R, Wei R P. Metall Mater Trans A. 1998; 29: 1145-1151.
- [40] Lorensen W E, Cline H E. Computer graphics (ACM). 1987; 21: 163-169.
- [41] Kalidindi S R, Bhattacharyya A, Doherty R D. Proc R Soc Lond A. 2004; 460: 1935-1956.
- [42] Huang X, Hansen N, Scripta Mater. 1997; 37: 1-7.
- [43] Thorning C, Somers M A J , Wert J A. Mater Sci. Eng. A 2005; 397: 215-228.
- [44] Narayanasamy R, Ramesh T and Prabhaker . Int. J. Adv. Manuf. Technol. 2009; 47: 295-311.
- [45] Li S F, Ling J, Hefferan C M, Pokharel R, Lienert U, Rollett A D and Suter R M J. Appl. Cryst. 2012; 45: 1098-1108
- [46] LeClere D J, Kamiko T, Mizuseki Y, Suzuki Y, Takeuchi A, Uesugi K, Kobayashi M, Toda H. Proc ICAA13 edited by Hasso Weiland, Anthony D. Rollett, William A.

Cassada. Pittsburgh PA USA: TMS; 2012: 9-14.

- Fig. 1 Schematic illustration of experimental and subsequent image processing processes in the grain boundary tracking technique.
- Fig. 2 Schematic illustration of the 3D image processing procedures in the grain boundary tracking process.
- Fig. 3 Details of the masking treatment for grain boundary mask preparation. (a) and (b) have been prepared with different linear absorption coefficient ranges, $\Delta\mu$, and threshold value, μ_c . (c) shows an extracted gallium-penetrated region, with grain boundaries and vicinity. A domain revealing grains is extracted as shown in (e), after applying dilation and erosion treatment.
- Fig. 4 A series of grain segmentation sub-processes in the grain boundary tracking process, in which missing grain boundary segments are recovered by utilising the watershed algorithm. (f) indicates an example of over-segmentation (white arrows) that occurs due to the presence of image noise and/or various irregularities that are shown in (a) by yellow arrows).
- Fig. 5 Typical example of the recovery of morphological information on a grain boundary, through application of the watershed algorithm. The images are 3D perspective views of sections of rendered grain boundary planes.
- Fig. 6 Nominal stress vs. nominal strain curve. The loading points at which 3D images are captured in the experiment are shown.

Fig. 7 Illustration of the grain boundary tracking of an actual grain in the 2024 aluminium alloy.

Fig. 8 Development of local strain distribution in Grains 1, 2, 3 and 4.

Fig. 9 Virtual cross-sections on which high strain was observed together with an equivalent strain map on the identical cross-section. One-dimensional strain values between particles P_1 and P_2 , P_1 and P_3 , and P_2 and P_3 are 0.108, 0.112 and 0.209, respectively.

Fig. 10 (a) Change in the grain morphology of Grain 4 (specified in Fig. 8) with loading, and (b) equivalent strain mapping on y-z cross-sections as specified in (a).

Fig. 11 Representation of displacement vectors ($\times 10$ scale) on the surface of Grain 4 (specified in Fig. 8). The blue and red arrows indicate the tensile and compression displacements of grain boundary particles, respectively.

Fig. 12 Examples of strain mapping on a virtual cross-section, representing the normal strain in the loading direction, ε_z , equivalent strain, ε_{eq} , hydrostatic strain, ε_h , and $\varepsilon_{eq}/\varepsilon_h$, between loading steps 0 and 5.

Fig. 13 Example of strain mapping, representing the interaction of three neighbouring grains in terms of $\varepsilon_{eq}/\varepsilon_h$, between loading steps 0 and 5.

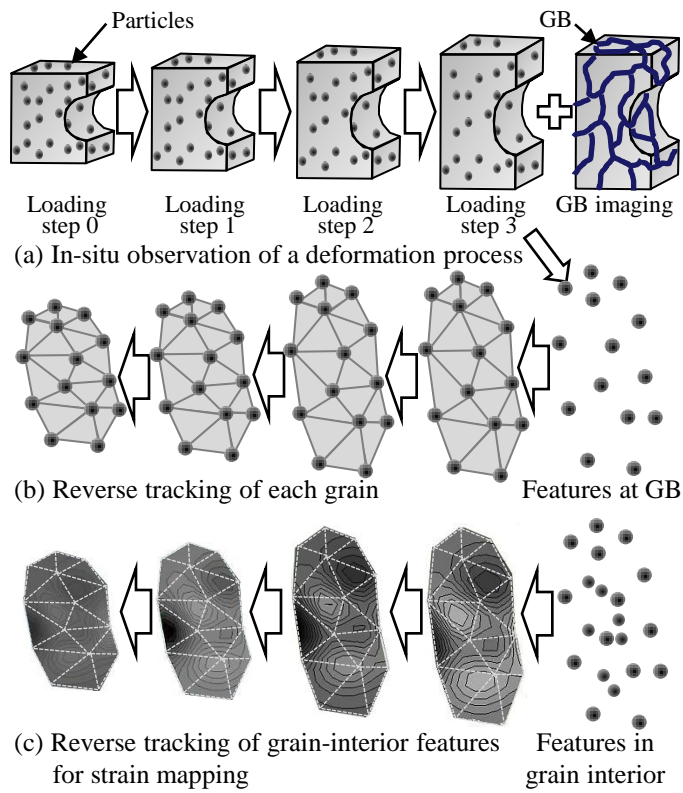


Fig. 1 Schematic illustration of experimental and subsequent image processing processes in the grain boundary tracking technique.

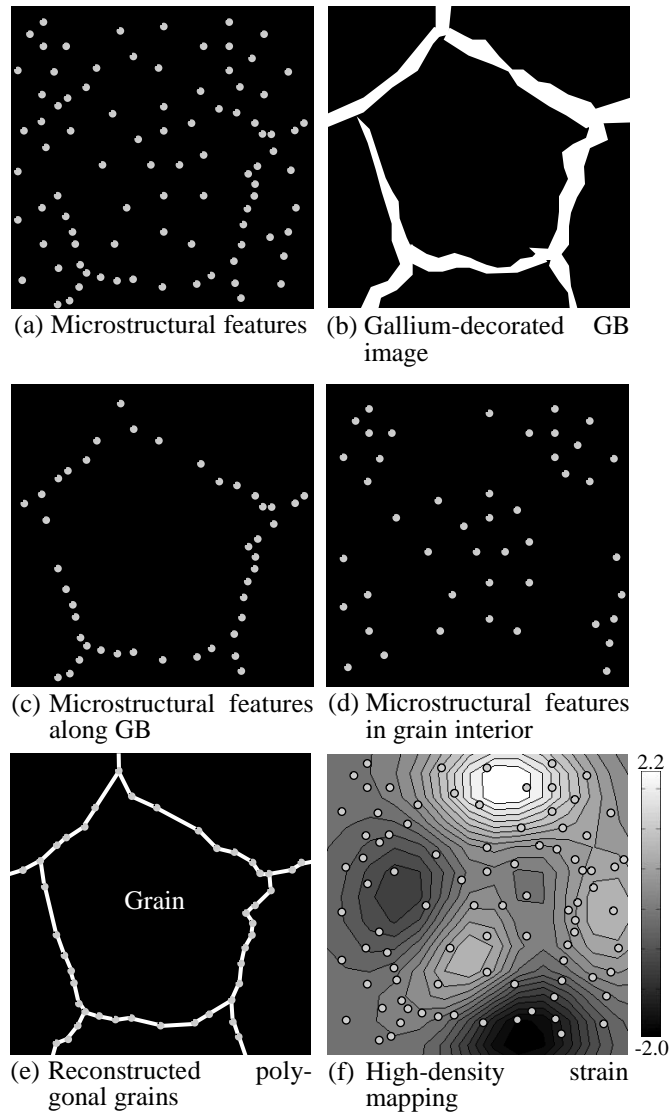


Fig. 2 Schematic illustration of the 3D image processing procedures in the grain boundary tracking process.

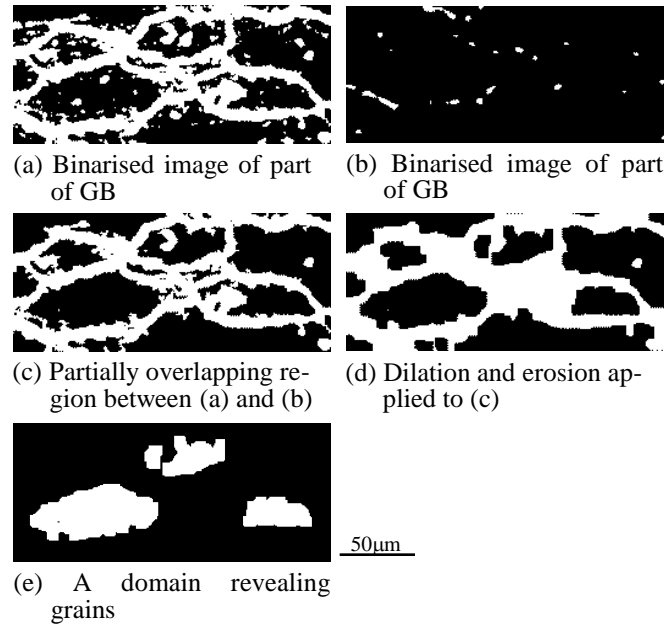


Fig. 3 Details of the masking treatment for grain boundary mask preparation. (a) and (b) have been prepared with different linear absorption coefficient ranges, $\Delta\mu$, and threshold value, μ_c . (c) shows an extracted gallium-penetrated region, with grain boundaries and vicinity. A domain revealing grains is extracted as shown in (e), after applying dilation and erosion treatment.

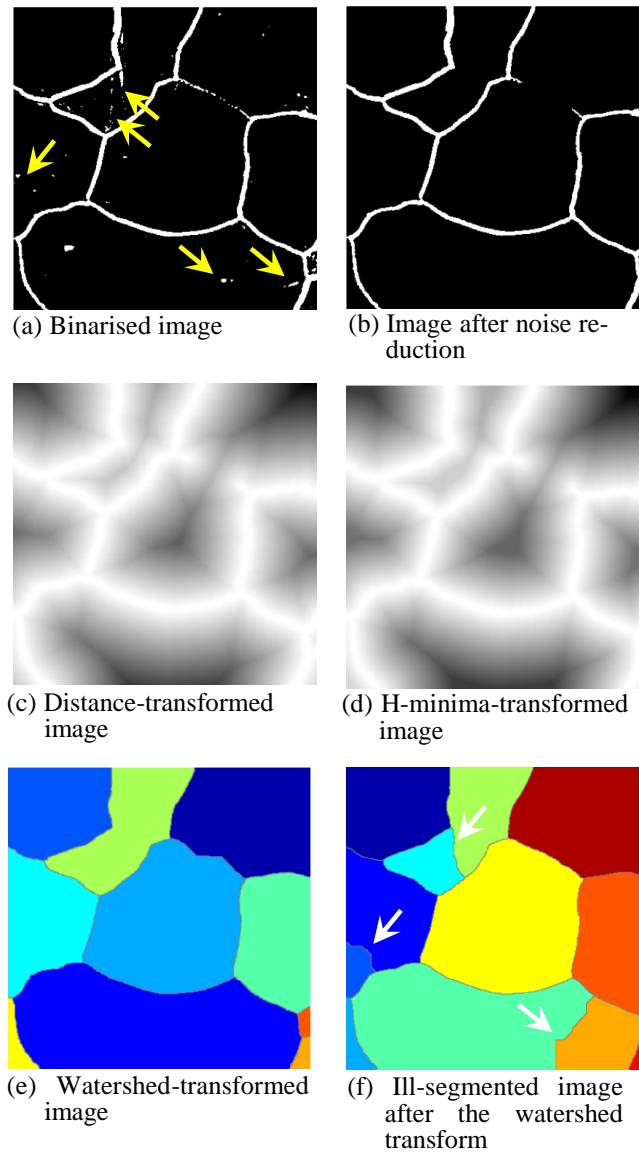


Fig. 4 A series of grain segmentation sub-processes in the grain boundary tracking process, in which missing grain boundary segments are recovered by utilising the watershed algorithm. (f) indicates an example of over-segmentation (white arrows) that occurs due to the presence of image noise and/or various irregularities that are shown in (a) by yellow arrows).

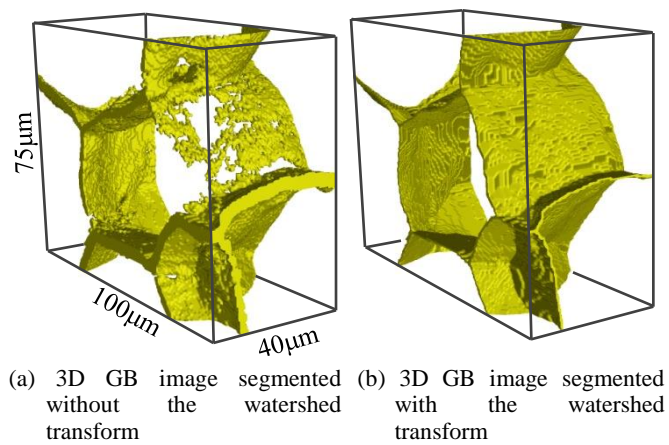


Fig. 5 Typical example of the recovery of morphological information on a grain boundary, through application of the watershed algorithm. The images are 3D perspective views of sections of rendered grain boundary planes.

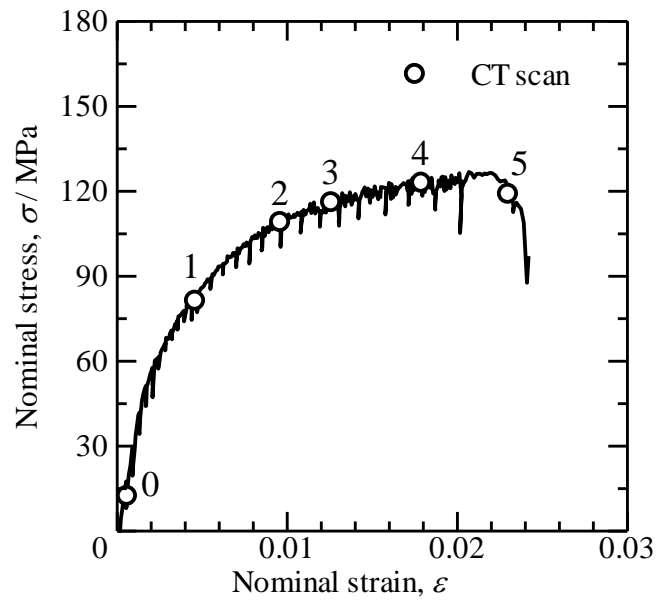


Fig. 6 Nominal stress vs. nominal strain curve. The loading points at which 3D images are captured in the experiment are shown.

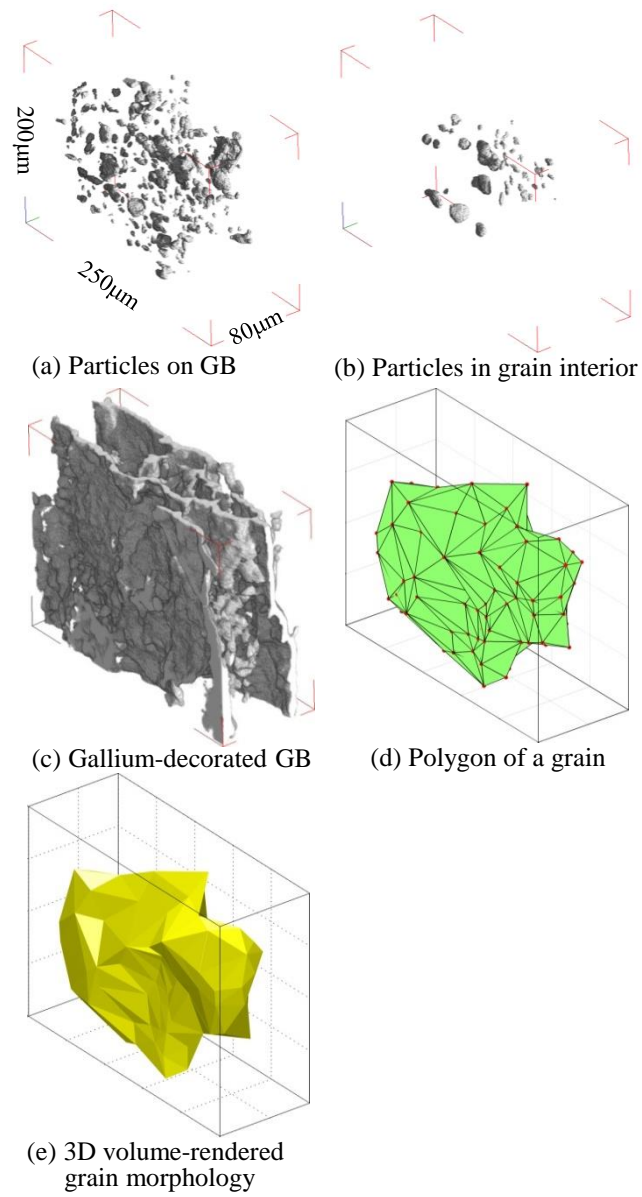


Fig. 7 Illustration of the grain boundary tracking of an actual grain in the 2024 aluminium alloy.

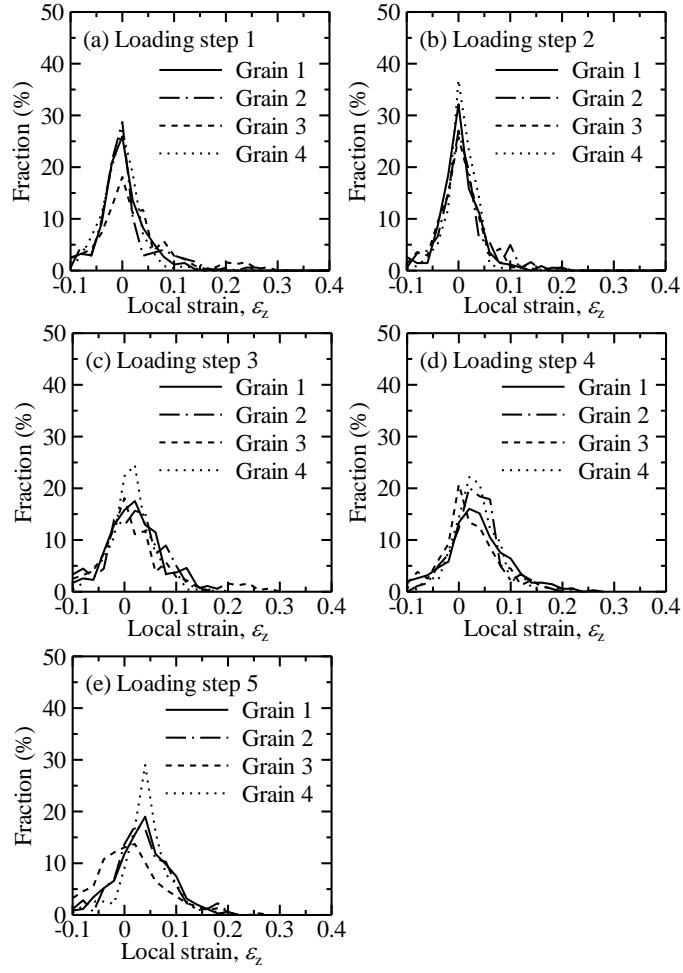


Fig. 8 Development of local strain distribution in Grains 1, 2, 3 and 4.

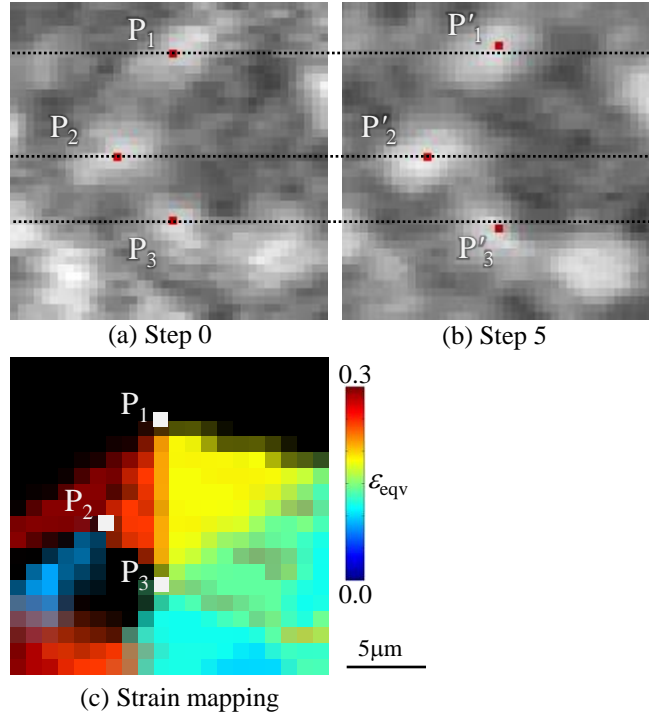


Fig. 9 Virtual cross-sections on which high strain was observed together with an equivalent strain map on the identical cross-section. One-dimensional strain values between particles P_1 and P_2 , P_1 and P_3 , and P_2 and P_3 are 0.108, 0.112 and 0.209, respectively.

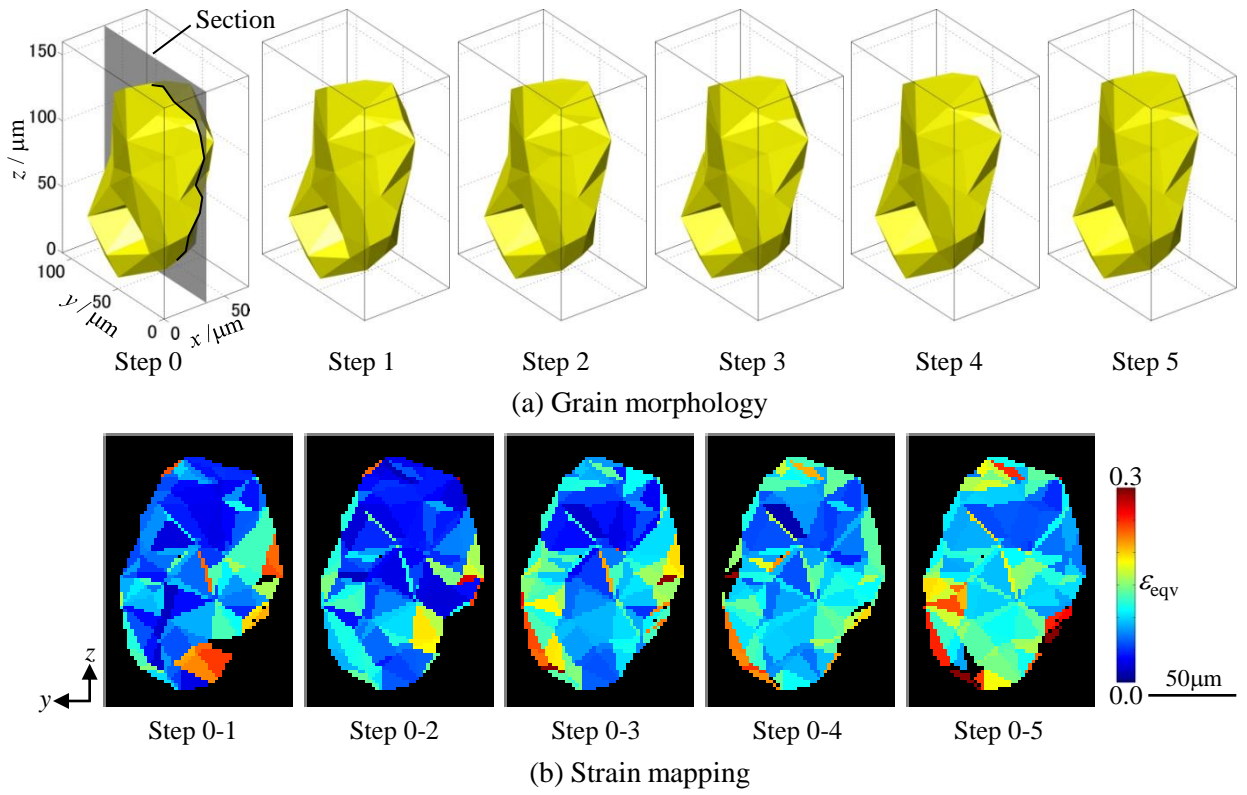


Fig. 10 (a) Change in the grain morphology of Grain 4 (specified in Fig. 8) with loading, and (b) equivalent strain mapping on y - z cross-sections as specified in (a).

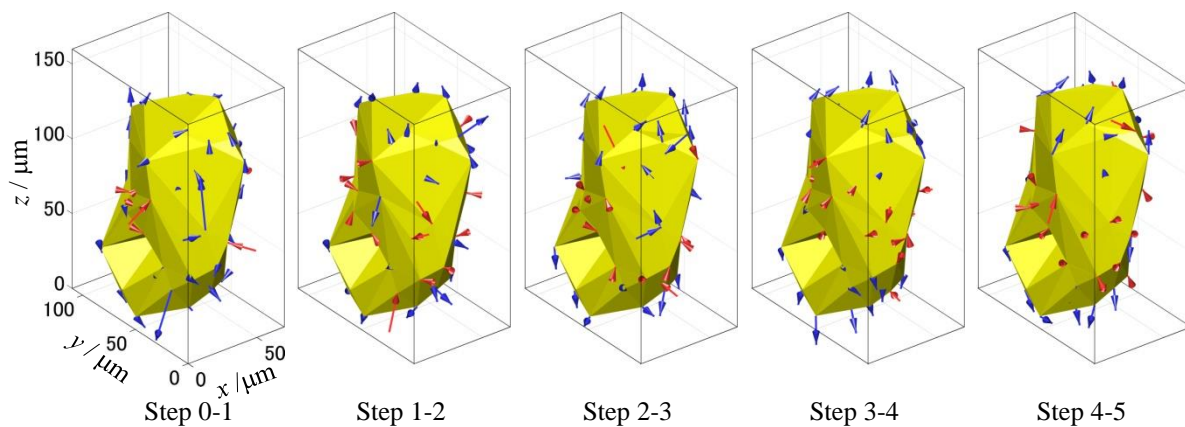


Fig. 11 Representation of displacement vectors ($\times 10$ scale) on the surface of Grain 4 (specified in Fig. 8). The blue and red arrows indicate the tensile and compression displacements of grain boundary particles, respectively.

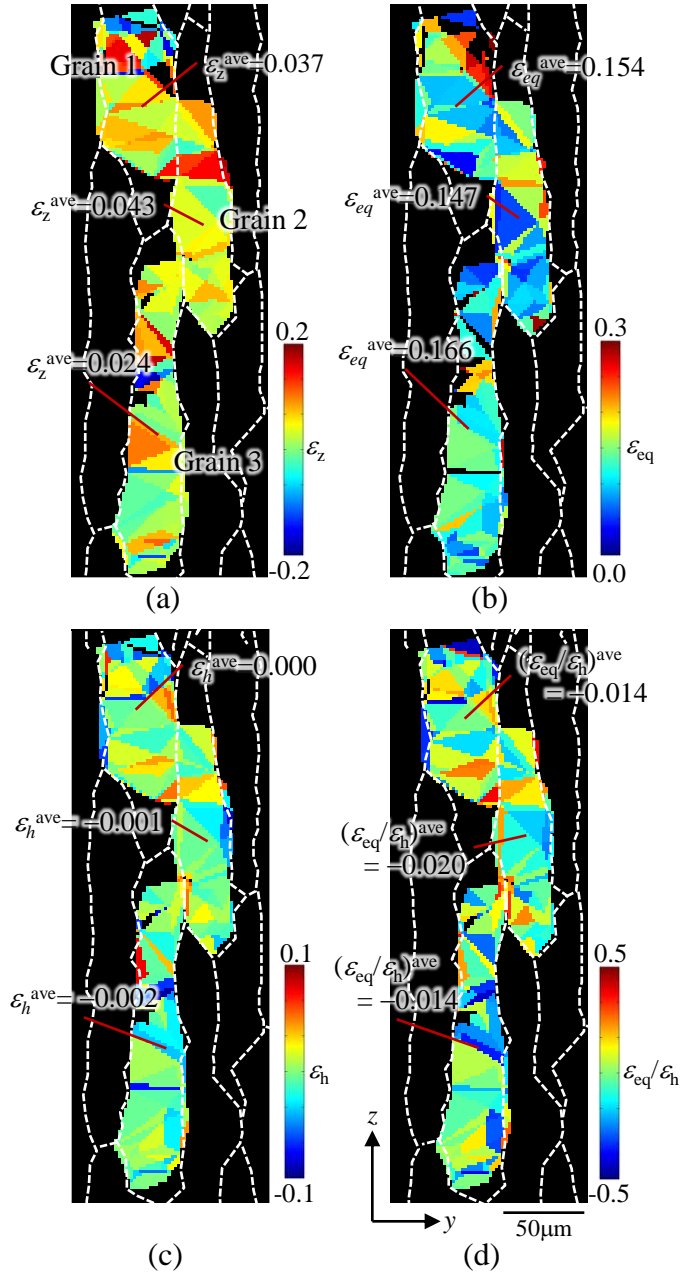


Fig. 12 Examples of strain mapping on a virtual cross-section, representing the normal strain in the loading direction, ε_z , equivalent strain, ε_{eq} , hydrostatic strain, ε_h , and $\varepsilon_{eq}/\varepsilon_h$, between loading steps 0 and 5.

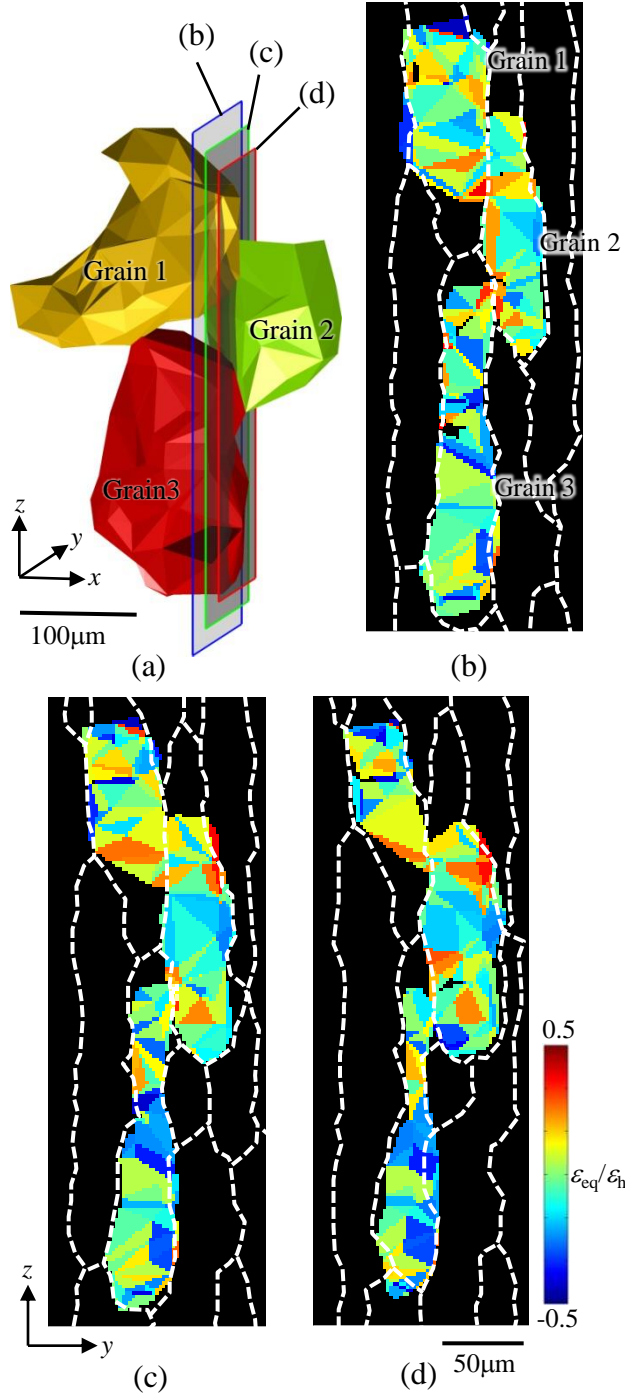


Fig. 13 Example of strain mapping, representing the interaction of three neighbouring grains in terms of ϵ_{cq}/ϵ_h , between loading steps 0 and 5.